Materials Advances

PAPER

Check for updates

Naphthalene–stilbenes as effective visible-light sensitizers to study the effect of diluent and nanofillers on *in situ* photopolymerization and 3D-VAT printing process†

Wiktoria Tomal,[a] Karolina Gałuszka,[a] Petr Lepcio, [ID][b] Maciej Pilch, [ID][a] Anna Chachaj-Brekiesz, [ID][c] Martina Korčušková[b] and Joanna Ortyl [ID]*[ad]

This study presents novel photoinitiating systems based on diaryliodonium salt (IOD) and 1-amino-4-methyl-6-styrylnaphthalene-2-carbonitrile derivatives developed as universal IOD photosensitizers. These systems' spectroscopic characteristics, electrochemical behavior, and thermodynamic parameters were investigated to determine the optimal two-component photoinitiating system for light-initiated polymerization, including free-radical and cationic reactions. This versatility in initiating both types of reactions was utilized to explore the dilution effect of non-reactive and two different reactive (cationic, free-radical) diluents. The best formulation was chosen according to Fourier-transform infrared spectroscopy (FTIR), photorheology, thermogravimetric analysis (TGA), and dynamic mechanical analysis (DMA) and tested for the preparation of functional nanocomposites with two types of nanofiller: silver oxide (Ag$_2$O) and hydroxyapatite (HA). The manufacturing process based on additive technology was analyzed according to FTIR spectroscopy and viscosity changes. The results show the high potential of the newly developed photosensitizers in practical applications and 3D-VAT printing.

1. Introduction

Light-initiated polymerization processes have consistently attracted interest from scientific and industrial communities for years due to the numerous advantages of this process, such as a high reaction rate, no need for solvents, and the ability to perform the reaction at room temperature.[1] Another reason is the large number of raw materials that can be used in the photopolymerization process, which can react according to different mechanisms: cationic[2–8] and free-radical[9–14] processes, reversible addition–fragmentation chain-transfer polymerization (RAFT),[15–19] or atom transfer radical polymerization (ATRP),[20–24] and can be both naturally and artificially produced. This large spectrum of monomers provides an opportunity to produce various functional polymeric materials in which

mechanical, thermal, and other parameters can be designed in advance.

It is well known that photoinitiators or initiating systems play a key role in light-initiated polymerization processes, which are responsible for initiating the photopolymerization process and influencing the reaction kinetics or the final properties of the cured polymer.[25–29] Rising environmental, safety and economic requirements are driving a constant search for photoinitiating systems that are progressively more efficient and better suited to demanding conditions. The properties of these systems include the best possible compatibility of their absorption characteristics with the emission characteristics of the used light sources, high initiation efficiency, and the presence of additives hindering the photopolymerization process.

As additive technologies continue to develop more rapidly, process improvements increasing the scope and feasibility of photopolymerization usage in 3D printing are being vigorously pursued by researchers.[30–37] 3D-VAT printing enables the production of three-dimensional polymer materials with a predetermined geometry while simultaneously having reasonable fabrication times and good control over the process.[38–41] In 3D-VAT printing, the type, amount, and form of the initiator/initiating system are particularly important for further applications.[42–46] The initiating system should provide a quick

[a] Cracow University of Technology, Faculty of Chemical Engineering and Technology, Warszawska 24, 31-155 Cracow, Poland.
E-mail: joanna.ortyl@pk.edu.pl

[b] Central European Institute of Technology, Brno University of Technology, Purkynova 656/123, Brno 61200, Czech Republic

[c] Jagiellonian University, Faculty of Chemistry, Gronostajowa 2, 30-387 Cracow, Poland

[d] Photo HiTech Ltd, Bobrzyńskiego 14, 30-348 Cracow, Poland

† Electronic supplementary information (ESI) available. See DOI: https://doi.org/10.1039/d3ma00943b

start to the process, ensuring reasonable printing time, should be sensitive to the light source, not causing overcrosslinking, and allow the highest possible precision and resolution of the printed objects. Both *in situ* polymerization and additive technologies imply specific requirements on monomers.[47,48] One of these is a sufficiently low viscosity to ensure smooth resin flow between exposed layers. Due to this limitation, many monomers cannot be used in 3D-VAT printing individually, although using a suitable diluent makes this possible. There are many types of reactive and non-reactive diluents, and studying their effects on photopolymerization and 3D printing is an integral part of the research into additive technologies.[49–52]

Another currently significant field is nanocomposites with various functional nano-sized fillers, which provide variable, tuneable, and often improved material properties.[53] Nano-additives can increase the mechanical tensile or compressive strength of materials,[54,55] increase their thermal[56,57] or electrical conductivity (*e.g.*, CNTs[58,59] and PEDOT[60]), and, for example, give them biocompatible or antibacterial properties.[61] The nano-additives certainly do not go unnoticed by the light-initiated polymerization processes: they can absorb or chemically react with other components, or significantly increase the overall viscosity, resulting in a complex change in the photocuring properties, such as the critical energy and penetration depth.[62,63] Therefore, the critical aspect for effective nanoresin curing and its possible application in 3D-VAT printing is an initiating system that can provide high process speed and eliminate the nanoadditive associated limitations.[64]

Accordingly, the following manuscript presents newly developed 1-amino-4-methyl-6-styrylnaphthalene-2-carbonitrile derivatives as highly efficient photosensitizers of diaryliodonium salts (Speedcure 938). Detailed spectroscopic, electrochemical, and thermodynamic analyses of these binary systems were performed to understand the inhibition mechanism and select the best systems for further studies. The photopolymerization process initiated by systems based on iodonium salt (IOD) and naphthalene–stilbene derivatives were investigated for the cationic photopolymerization reaction of an epoxy monomer and the free-radical polymerization of an acrylic monomer. The versatility of the proposed photoinitiating systems also allowed for a detailed analysis of the diluent effect on the radical photopolymerization and 3D-VAT printing processes, including the printed polymers' final properties. Three different systems containing both reactive and non-reactive diluents were analyzed: reactive diluent reacting according to the free-radical mechanism – isobornyl acrylate (IBOA), non-reactive diluent – ethylene glycol (MEG), and reactive diluent reacting according to the cationic mechanism – 1,6-hexanediol diglycidyl ether (HDEG). The best formulation was selected based on a detailed analysis of the photoconversion kinetics using techniques such as real-time FTIR or photorheology and mechanical testing. Furthermore, it was used to prepare functional nanocomposites containing silver oxide (Ag$_2$O) and hydroxyapatite (HA) nanofillers. The effects of nanoparticle type and concentration on the photopolymerization kinetics were investigated, and the applicability of these nanocomposites in 3D-VAT technology was determined.

2. Materials and methods

2.1. Materials

Bis-(4-*t*-butylphenyl)iodonium hexafluorophosphate (IOD; Lambson Ltd, Wetherby, UK) was used in this study as a commercially available photoinitiator. A bifunctional epoxy monomer, 4-epoxy-cyclohexylmethyl-3,4-epoxycyclohexane-carboxylate (CADE, from Lambson Ltd, Wetherby, UK), was used for the monomer reaction according to the cationic mechanism. A bifunctional aliphatic urethane diacrylate (Ebecryl® 4858, Allnex GMBH) was used as the monomer reacting according to the free-radical mechanism. The following compounds were used as diluents for the Ebecryl4858 monomer: isobornyl acrylate (IBOA, Allnex GMBH), ethylene glycol (MEG, Sigma Aldrich), and 1,6-hexanediol diglycidyl ether (HDEG, Sigma Aldrich). A commercial thioxanthone derivative was used as a reference photosensitizer: 2-ethyl-9,10-dimethoxyanthracene (DTHX, from Sigma Aldrich). The structures of all the compounds used in this study are shown in Fig. 1. As functional nanofillers the following fillers were used: hydroxyapatite (HA) in the form of acicular powder (from Sigma Aldrich, purity ≥96%, particle size: 60 nm ± 10 nm) and silver oxide: spherical shape nanoparticles (from Sigma Aldrich, purity = 99%, particle size: 20–80 nm).

Newly developed 1-amino-4-methyl-6-styrylnaphthalene-2-carbonitrile derivatives were used as sensitizers for the iodonium salt: 1-amino-4-methyl-6-[(*E*)-styryl]naphthalene-2-carbonitrile (NS), 1-amino-6-[(*E*)-2-(4-cyanophenyl)vinyl]-4-methylnaphthalene-2-carbonitrile (NS-CN), 1-amino-4-methyl-6-[(*E*)-2-(4-methylphenyl)-vinyl]naphthalene-2-carbonitrile (NS-Me), 1-amino-4-methyl-6-[(*E*)-2-(4-methylsulfanylphenyl)vinyl]naphthalene-2-carbonitrile (NS-S-Me), 1-amino-6-[(*E*)-2-(4-fluorophenyl)vinyl]-4-methylnaphthalene-2-carbonitrile (NS-F), 1-amino-6-[(*E*)-2-(4-methoxyphenyl)vinyl]-4-methylnaphthalene-2-carbonitrile (NS-O-Me), 1-amino-6-[(*E*)-2-(4-chlorophenyl)vinyl]-4-methylnaphthalene-2-carbonitrile (NS-Cl), and 1-amino-6-[(*E*)-2-(4-tert-butoxyphenyl)vinyl]-4-methylnaphthalene-2-carbonitrile (NS-O-(Me)$_3$). All target compounds (NS, NS-ME, NS-F, NS-Cl, NS-CN, NS-S-Me, NS-O-Me, NS-O-(Me)$_3$) were synthesized using Heck coupling of 1-amino-6-bromo-4-methylnaphthalene-2-carbonitrile with an appropriate styrene derivative. The applied synthetic protocol has already been described in the literature for Heck coupling of 2-amino-4-(4-bromophenyl)-6-phenyl-benzene-1,3-dicarbonitrile.[65] A detailed description of the synthesis of these derivatives, along with ^{1}H-NMR (Fig. S1–S8, ESI†) and LC-MS analyses of the obtained structures, are provided in the ESI.† The structures of the eight synthesized naphthalene–stilbene derivatives are shown in Fig. 2.

2.2. Spectroscopic characterization of naphthalene–stilbene derivatives

The absorption characteristics of the 1-amino-4-methyl-6-styrylnaphthalene-2-carbonitrile derivatives were studied using a Silver Nova spectrometer (StellarNet Inc., USA) with a range of 190–1100 nm, equipped with a broadband deuterium-halogen UV-Vis light source. The absorbance of the compounds was studied in acetonitrile at room temperature using a quartz cuvette with a 10 mm optical path length.
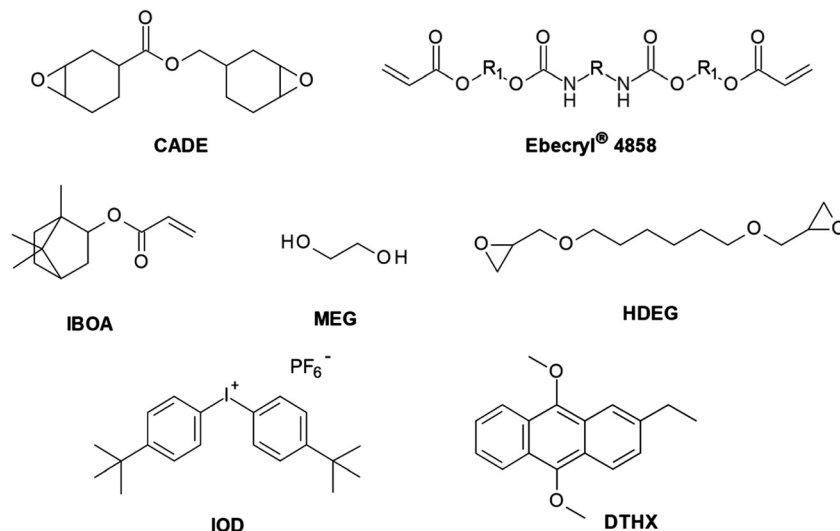
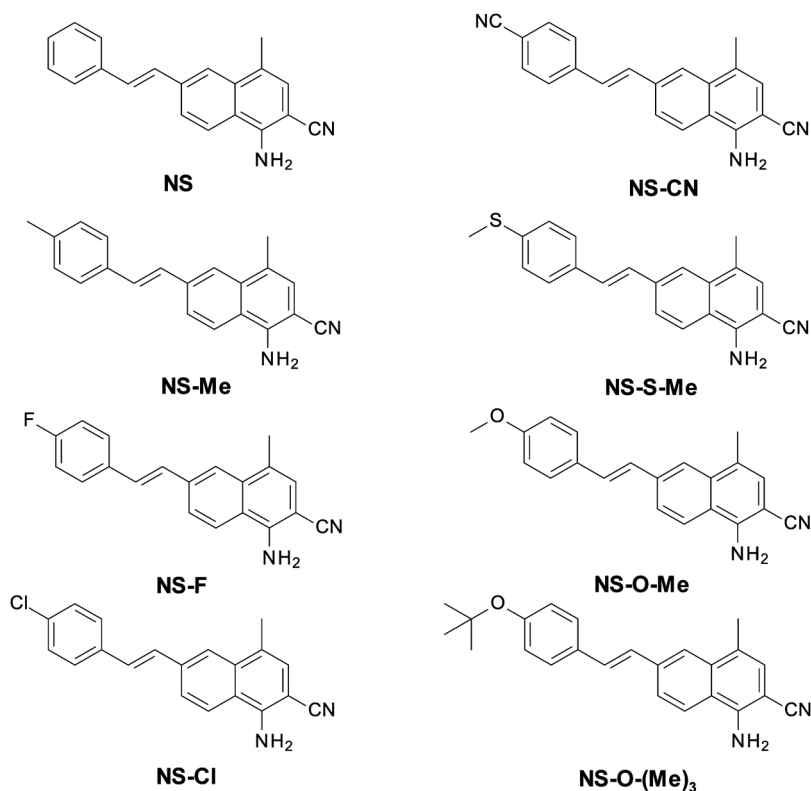**Fig. 1** Structures of the monomers and additives used in the study.

Fig. 2 Structures of the 1-amino-4-methyl-6-styrylnaphthalene-2-carbonitrile derivatives used in the study.

The photostability of naphthalene–stilbene derivatives under irradiation with 405 nm light was measured using the same Silver Nova spectrometer (as above), and the measurement was performed for acetonitrile solutions of the photosensitizers alone as well as together with the Speedcure 938 photoinitiator (IOD) (the salt concentration was 2.7×10^{-2} mol dm^{-3}). During the measurement, the cuvette with a given solution was irradiated using a 405 nm Vis-LED and

a current of 1000 mA (Thorlabs Inc., Tampa, FL, USA) for 30 or 10 min.

The fluorescence quenching of the investigated derivatives in acetonitrile was measured to determine the reactivity of the proposed two-component initiator system. The intensity of the fluorescence spectrum of 1-amino-4-methyl-6-styrylnaphthalene-2-carbonitrile derivatives was measured in the presence of the quencher iodonium salt (IOD with a concentration of

2.7×10^{-2} mol dm^{-3}), which was added to the solution containing the NS derivative. A Fluoromax^{+TM} spectrofluorometer (Horiba) was used for the fluorescence studies. To quantitatively describe the fluorescence quenching of photosensitizer molecules by IOD, the Stern–Volmer constant (K_{SV}) was determined using the following formula:

$$K_{SV} = \frac{I_0 \cdot I - 1}{C_{IOD}} \qquad (1)$$

where I_0 and I are the fluorescence intensities of the photosensitizer in the absence and presence of IOD, respectively, and C_{IOD} is the concentration of the iodonium salt.

2.3. Electrochemical and thermodynamical analysis of photosensitizers

The oxidation (E_{ox}) and reduction potentials (E_{red}) of the tested 1-amino-4-methyl-6-styrylnaphthalene-2-carbonitrile derivatives were measured in acetonitrile by cyclic voltammetry using an M161E electrochemical analyzer and an M164D electrode stand (MTM, Poland). During the measurement, tetrabutylammonium hexafluorophosphate (1 M) (Sigma Aldrich) was used as the basic electrolyte, a platinum plate was used as the working electrode, and a silver electrode (Ag/AgCl) was used as the reference electrode. The scanning rate was 0.1 V s^{-1}, using ferrocene as the standard, and the potentials were determined from the mid-peak potentials. The Gibbs free energy (ΔG_{et}) change during the electron transfer process in the two-component initiating system was calculated based on the resulting potentials. ΔG_{et} was determined using the classical Rehm–Weller eqn (2):

$$\Delta G_{et} = F[E_{ox}\,(D/D^{\bullet+}) - E_{red}\,(A^{\bullet-}/A)] - E_{00} - (Ze^2/\varepsilon a) \qquad (2)$$

where $E_{ox}\,(D/D^{\bullet+})$ is the oxidation potential of the electron donor, $E_{red}\,(A^{\bullet-}/A)$ is the electron acceptor reduction potential, E_{00} is the excited-state energy, and $(Ze^2/\varepsilon a)$ is the electrostatic interaction energy, whose value is negligible in polar solvents. The energy of the singlet excited state (E_{00}) was determined from the excitation and emission spectra obtained using a spectrofluorometer Fluoromax^{+TM} (Horiba Scientific).

2.4. Real-time FTIR

The main objective of this study was to determine the suitability of 1-amino-4-methyl-6-styrylnaphthalene-2-carbonitrile derivatives for initiating cationic and free-radical photopolymerization processes (along with iodonium salt). The suitability of the proposed photoinitiating systems was determined for different compositions, and the concentration of the individual components of the photoinitiating system was determined as a weight concentration calculated in relation to the amount of used monomer or monomer-diluent mixture. A real-time FTIR method used a spectrophotometer FTIR^{i10} NICOLET^{TM} (Thermo Scientific) equipped with a horizontal adapter to analyze the kinetics of the light-initiated polymerization process, a. Vis-LED with an emission wavelength of $\lambda_{max} = 405$ nm or $\lambda_{max} = 415$ nm was applied as a light source. All measurements and sample handling were carried out in a red-light room. The OMNIC program dedicated to processing FT-IR spectra was used to monitor the polymerization reaction. The conversion rate of the monomer was calculated from eqn (3):

$$\text{Conversion}[\%] = \left(1 - \frac{A_{After}}{A_{Before}}\right) \times 100\% \qquad (3)$$

where A_{After} is the value of the band area monitored during the photopolymerization process as a function of time, and A_{Before} is the initial value of the area of the band at the monitored wavenumber. The ranges of the wave numbers used for monitoring the reaction progress are given below for each reaction.

2.4.1. Cationic photopolymerization kinetics of the epoxy ring opening reaction. The effectiveness of the developed photosensitizers was tested for their suitability to initiate cationic polymerization of the CADE epoxy monomer in the presence of IOD. The experimental two-component system contained iodonium salt IOD (1% by weight) and a naphthalene–stilbene derivative (0.1% by weight) relative to the amount of CADE monomer. The following system was used as references: CADE + IOD (1.0 wt%) + DTHX (0.1 wt%). A drop of the prepared mixture was placed on a barium fluoride pastille with a diameter of $\phi = 25 \pm 0.2$ mm $\times$ 5 $\pm$ 0.1 mm, which was then placed in a horizontal attachment of the FTIR spectrometer. Measurements were performed while maintaining the same thickness of the applied composition layer of 25 μm. The degree of epoxy monomer conversion was monitored at 790 cm^{-1}, corresponding to epoxy groups. The measurements were performed for 400 s at a constant temperature of 25 °C.

2.4.2. Free-radical photopolymerization kinetics of acrylate monomer reaction. 1-Amino-4-methyl-6-styrylnaphthalene-2-carbonitrile derivatives were also tested for their sensitizing effectiveness with iodonium salts to initiate free-radical photopolymerization. The commercially used diacrylate monomer Ebecryl® 4858 and a two-component initiating system, IOD (1.0 wt%) and naphthalene–stilbene derivative (0.1 wt%), were used for this purpose. The following system was used as references: Ebecryl® 4858 + IOD (1.0 wt%) + DTHX (0.1 wt%). The polymerization process was carried out under oxygen-free conditions by layering the composition between the two polypropylene films while maintaining a constant sample thickness of 25 μm. The degree of acrylate monomer conversion was monitored for the peak for which the maximum occurs at 1635 cm^{-1}, corresponding to C=C double bonds. The measurements were performed for 600 s at a constant temperature of 25 °C.

2.4.3. Effect of diluent type on the free-radical photopolymerization kinetics. The diluent effect on the Ebecryl® 4858 photopolymerization kinetics initiated by a two-component initiating system of IOD–naphthalene stilbene derivative was studied due to its high viscosity. Three types of diluents were analyzed: (1) a reactive diluent reacting according to a free-radical mechanism: Ebecryl® 4858/IBOA (0.7/0.3 w/w) + IOD (3.0 wt%)/NS (0.1 wt%); (2) a non-reactive diluent: Ebecryl® 4858/MEG (0.7/0.3 w/w) + IOD (3.0 wt%)/NS (0.1 wt%); (3) a reactive diluent reacting according to the cationic mechanism: Ebecryl® 4858/HDEG (0.7/0.3 w/w) + IOD (130 wt%)/NS (0.1 wt%). Measurements were carried out as described above:

between two polypropylene films securing the sample thickness of 25 μm, the measurement time was 400 s, and acrylate conversions were monitored for the peak for which the maximum occurs at 1635 cm^{-1}.

2.4.4. Photopolymerization kinetics of functional nanocomposites. The process of obtaining the nanocomposites was also analyzed using real-time FTIR. Two types of photosensitive formulations containing different concentrations of nanoadditives were studied. The base of these compositions was a mixture of Ebecryl® 4858/IBOA (0.7/0.3 w/w) and IOD (3.0 wt%)/NS (0.1 wt%). Two types of functional nanoadditives were tested: silver oxide (Ag_2O) with weight concentrations: 1%, 2%, and 5%, and hydroxyapatite (HA) with weight concentrations: 2%, 5%, and 10%. Measurements were carried out for 600 s in an oxygen-limited environment by applying a drop of nanoresin between the two polypropylene films while maintaining a constant sample thickness of 25 μm. The progress of the nanocomposites was monitored for the peak for which the maximum occurs at 1635 cm^{-1} corresponding to the C=C bonds present in the monomers.

2.5. Study of the rheological behavior during the photopolymerization process

Photorheological measurements were carried out to compare the influence of the diluent type and the type and amount of functional nanoadditives on the photopolymerization process. The formulations' dynamic viscosity and kinetic parameters of the photopolymerization process, such as induction time, gel point, and polymerization shrinkage, were determined based on these results. The induction time was determined as the time difference between starting the light exposure and detecting an abrupt increase in viscosity. The gel point was determined as the storage and loss moduli crossover point. The shrinkage was determined according to the following formula:

$$\text{Shrinkage}[\%] = \left(1 - \frac{d_{\text{After}}}{d_{\text{Before}}}\right) \times 100\% \qquad (4)$$

where d_{Before} and d_{After} represent the gap, *i.e.*, the distance between the upper and lower photorheometer geometries, at the start and end of the photopolymerization process, respectively.

Rheological behavior was studied using a Physica MCR 302 rheometer (Anton Paar) equipped with parallel plate geometries with a diameter of 20 mm. The bottom geometry by the Bluepoint LEC eco system (Hönle UV Technology) was quartz,

allowing light exposure and in-situ photocuring. In the experiments, a 405 nm wavelength diode with a light intensity of 5.4 mW cm^{-2} was used, and this value was controlled with a PM160 – Si Sensor Power (Thorlabs Inc.). Photorheological oscillatory experiments were conducted using the following parameters: the nominal distance between the top and bottom geometries of the system (gap) was 0.1 mm, the frequency was 1.0 Hz, the strain amplitude was 1.0%, and the process was carried out under isothermal conditions (at 25 °C). A 60 second dark period was used to stabilize the sample, after which the light was turned on.

2.6. 3D-VAT printing experiments

A model was designed to determine the X–Y–Z resolution, allowing us to compare the diluent type effect on the printing process, as well as on the final properties of the resulting 3D printed polymeric material (Fig. 3a). On the other hand, the gyroidal cylinder model presented in Fig. 3b was used to obtain functional nanocomposite materials. All models were drawn using Fusion 360® software (AutoDesk) in a stereolithography format (.stl). The diluent effect was studied using an Anycubic Photon Ultra, a DLP VAT photopolymerization 3D printer equipped with a projector that emits light with a wavelength of 405 nm as a light source. In this case, the models were sliced using the Anycubic Photon Slicer software (Anycubic). Nanocomposite samples were printed with a Lumen X$^{+™}$ printer (CellInk Inc.), which also has a projector emitting light at 405 nm, slicing the models directly in the printer using Volumetric® software.

The printing parameters for both models and different photoformulation mixtures are given in the ESI† in Tables S1 and S2, and the values were determined from Jacob's working curves.

2.6.1. Jacob's working curves and determination of the printing parameters. Jacob's working curves were used to determine key printing parameters, such as the critical energy required to cure an infinitely thin solid layer (E_c) and the penetration depth penetration (D_p), according to formula (5):

$$C_d = D_p \ln\left[\frac{E_0}{E_c}\right] \qquad (5)$$

where C_d is the thickness of the cured layer, and E_0 is the exposure energy used to cure the layer (multiplication of printer power (5 mW cm^{-2}) and curing time).
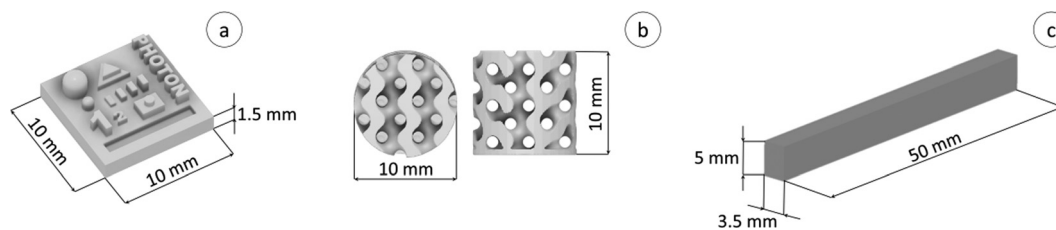

Fig. 3 (a) 3D view of the created design used for X–Y–Z resolution; (b) gyroidal model designed for the manufacturing of nanocomposites; (c) specimens for the DMA study.

In order to prepare Jacob's working curves, a computer model with dimensions in the X and Y axis of 10 mm was prepared, which was then used to prepare individual slices of printed material at different exposure times to light. In order to allow free light penetration through the resin, the printing process was carried out without a platform, and the printer's bath was filled to a height of 1.5 cm so as not to limit the material's curing depth. Then, using different crosslinking times, materials were printed in the form of a rectangular shape with known dimensions in the X- and Y-axis, *i.e.* 10 mm, and the dimension in the Z-axis was determined experimentally by measuring the thickness of the print with a micrometer screw in five places.

C_d was established by curing single-layer squares with x- and y-axis dimensions of 10 mm in the absence of the printing platform, *i.e.*, unrestricted in the z-axis, and manually measuring the cured thickness with a micrometer. The averaged C_d was plotted in the log-norm graph as $C_d = f(E_0)$ to determine D_p as the slope of the working curve and E_c as its intersection with the x-axis.

2.7. Analysis of three-dimensional printouts of different compositions

2.7.1. Resolution analysis using an optical microscope. A DSX1000 digital microscope with a DSX10-SXLOB3X objective with 42–420× magnification (Olympus) was used to observe 3D printouts containing various reactive and non-reactive diluents and to analyze materials with different types and concentrations of functional nano-additives. The printing resolution was determined as the capability to print the fine details of varying thicknesses included in the model. The printing precision was evaluated by comparing the modeled and experimentally determined dimensions.

2.7.2. Scanning electron microscope. A scanning electron microscope Mira 3 XMU (Tescan, Czech Republic) was used to visualize the morphology of the nanocomposite printouts. Before the measurements, the samples were sputter-coated with a 12 nm gold layer using an ACE 600 coating machine (Leica, Germany) to make them electrically conductive and prevent their charging. Micrographs were taken at various magnifications using a standard Everhart–Thornley secondary electron (SE) detector and a low-energy backscattered electron (BSE) detector while maintaining an accelerating voltage of 10 kV.

2.7.3. Dynamic mechanical analysis (DMA). The mechanical properties were assessed through hybrid dynamic mechanical analysis (DMA) combined with a heat deflection temperature measurement (HDT).[30] It was performed in a 3-point bending setup with an oscillatory frequency of 1 Hz and a dynamic oscillation strain of 0.002% superimposed with small static stress of 0.455 MPa using an RSA-G2 machine (TA Instruments, USA). The storage (E') and loss moduli (E''), and loss tangent ($\tan \delta = E''/E'$) were obtained as a function of temperature between $-30\ ^\circ$C and 160 $^\circ$C at a controlled heating rate of 2 $^\circ$C min^{-1}. The glass transition temperature (T_g) was determined at the maximum of the $\tan \delta$ curve. The heat deflection temperature (HDT) was determined at deflection corresponding to 0.195% flexural strain ε_f (about 0.25 mm), given by eqn (6):

$$\varepsilon_f = \frac{600 \cdot s \cdot h}{L^2} \qquad (6)$$

where s is the deflection, h is the specimen's thickness, and L is the geometry span (40 mm). The network density (υ_e) was determined by measuring the modulus in the rubbery region at temperatures above T_g according to eqn (7):

$$\upsilon_e = 2(1 + \upsilon) \cdot \frac{G_N^0}{RT} \qquad (7)$$

where υ is the Poisson's ratio ($\upsilon = 0.5$ for incompressible material), G_N^0 is the rubber-plateau modulus, T is the thermodynamic temperature, and R is the gas constant.

2.7.4. Thermogravimetric analysis (TGA). Thermogravimetric analysis was performed as a simple temperature ramp in a non-oxidative nitrogen atmosphere from ambient temperature to 700 $^\circ$C at a heating rate of 10 $^\circ$C min^{-1} using Discovery TGA (TA Instruments, USA). The sample size was typically around 10 mg. A differential thermogravimetric signal was obtained as the first derivative of the residual weight signal in the TRIOS OEM software.

3. Results and discussion

3.1. Spectroscopic analysis of naphthalene–stilbene derivatives

The application study of the synthesized 1-amino-4-methyl-6-styrylnaphthalene-2-carbonitrile derivatives determined their spectroscopic properties and potential to act as photosensitizers. The commercially used iodonium salt Speedcure 938 (IOD) and its derivatives exhibit absorption characteristics extending into the UV-A range. Because of the new safety standards and awareness of UV-light harmfulness, the chemical industry is slowly replacing the previously dominant mercury lamps with light-emitting diodes (LEDs). This change has resulted in a mismatch between the absorption characteristics of these commercial cationic initiators and the emission characteristics of modern LED light sources. Consequently, the search for sensitizers with a suitable absorption range extending to wavelengths in the visible range (>400 nm) that, together with iodonium salts, will effectively initiate the polymerization process, is a priority for many researchers. The absorption characteristics of the 1-amino-4-methyl-6-styrylnaphthalene-2-carbonitrile derivatives synthesized within the scope of this manuscript were measured in acetonitrile, and the results, in the form of the molar extinction coefficient dependence on the wavelength, are shown in Fig. 4.

As shown, the proposed naphthalene–stilbene derivatives exhibit excellent absorption characteristics, reaching a wavelength of $\lambda_{max} \approx 450$ nm, making them good candidates for use in two-component initiating systems along with iodonium salt (IOD). These derivatives have a high molar extinction coefficient at 405 nm and 415 nm, ranging between 2425–4234 dm^3 mol^{-1} cm^{-1} and 1177–2253 dm^3 mol^{-1} cm^{-1}, respectively. The exact
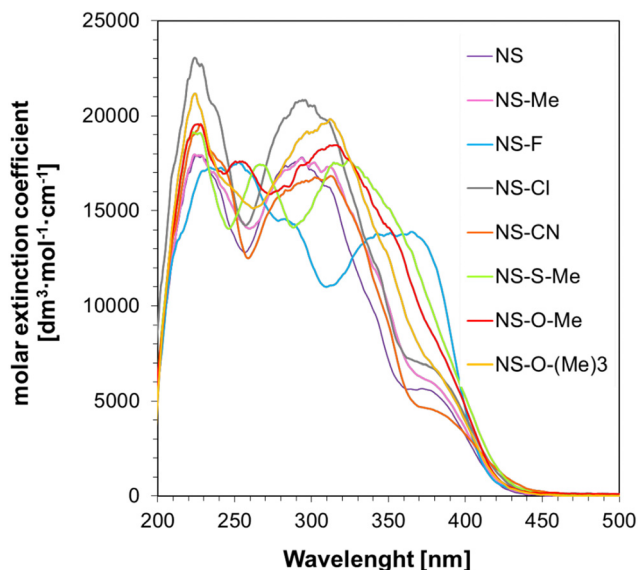
Fig. 4 UV-visible absorption spectra of 1-amino-4-methyl-6-styryl-naphthalene-2-carbonitrile derivatives in acetonitrile (ACN).

values of the ε coefficients for the different wavelengths are listed in Table 1.

3.2. Electrochemical and thermodynamical analysis of photosensitizers

In this study, 1-amino-4-methyl-6-styrylnaphthalene-2-carbonitrile derivatives are proposed as photosensitizers of iodonium salt (IOD). Through oxidative processes, they can initiate photopolymerization in this binary system due to electron transfer reactions in the photoexcited state. Naphthalene–stilbene derivatives absorb light and transfer electrons to an iodonium salt moiety. Therefore, selecting such photosensitizers to absorb light in the desired range (visible range) and have a high molar absorption coefficient for these wavelengths is crucial. Naphthalene–stilbene derivatives act as electron donors in this system, getting oxidized during the reaction. On the other hand, the diaryl iodonium salt (IOD) in its ground state is an electron acceptor. It is reduced due to electron transfer from the sensitizer molecule, and the compound decomposes into radicals. Further reduction of the iodonium cation leads to the formation of secondary radicals capable of initiating free-radical polymerization reactions. In turn, the iodonium salt anion can decompose into strong protonic acids

capable of initiating cationic polymerization reactions. Accordingly, the proposed system of diaryliodonium salt IOD and naphthalene–stilbene derivatives is an example of a versatile initiating system capable of photoinitiating different types of polymerization reactions: free radical photopolymerization and cationic photopolymerization.

Thus, to determine the suitability of the developed photo-initiating systems, naphthalene–stilbene derivatives – iodonium salt, their oxidation potentials were determined by cyclic voltammetry (Fig. S9–S19, ESI†). The reduction potentials of these compounds were also determined, and the Gibbs free enthalpy (ΔG_{et}) of the electron transfer process in this system was calculated. The electron transfer process occurs according to the photoreduction mechanism in systems such as the amine derivative of naphthalene–stilbene. Because only three of the investigated derivatives showed the ability to be reduced, these values were not satisfactory in terms of initiating the polymerization reaction; further considerations focused only on the analysis of the electron transfer process according to the photo-oxidation mechanism. The experimental data obtained from cyclic voltammetry measurements and the calculated Gibbs free enthalpies (ΔG_{et}) of the electron transfer process are summarized in Table 2.

The proposed 1-amino-4-methyl-6-styrylnaphthalene-2-carbonitrile derivatives have strong oxidizing abilities, with oxidation potentials in the 1107–1350 mV range. In addition, the free electron transfer enthalpy (ΔG_{et}) determined based on the Rehm–Waller equation in the naphthalene–stilbene derivative-iodonium salt combination has significantly negative values. This confirms the thermodynamic permissibility of the electron transfer from the photosensitizer to the diaryl iodonium salt molecule. The results of the fluorescence quenching experiment of the tested 1-amino-4-methyl-6-styrylnaphthalene-2-carbonitrile derivatives under the influence of the added quencher in the form of IOD salt provided additional confirmation of this theory. Changes in the fluorescence intensity of naphthalene–stilbene derivatives, depending on the concentration of the quencher, are shown in Fig. S28–S43 (ESI†). The Stern–Volmer constant was determined from the experimental results according to eqn (1), and the obtained values are summarized in Table 2. It was concluded that dynamic quenching of the photosensitizer's excited state by IOD occurs in this two-component initiating system. The observed quenching reaction is linear: the fluorescence intensity of the NS derivatives decreases linearly with increasing concentration of the

Table 1 Spectral characteristics of the 1-amino-4-methyl-6-styrylnaphthalene-2-carbonitrile derivatives studied in acetonitrile

Acronym	Molar mass [g mol^{-1}]	ε^a @365 [dm^3 mol^{-1} cm^{-1}]	ε^a @405 nm [dm^3 mol^{-1} cm^{-1}]	ε^a @415 nm [dm^3 mol^{-1} cm^{-1}]
NS	284.1	5600	2400	1200
NS-Me	298.1	6650	2800	1400
NS-F	302.1	13 900	3000	1200
NS-Cl	318.1	7200	3400	1900
NS-CN	309.1	5000	2800	1800
NS-S-Me	330.1	12 800	4200	2250
NS-O-Me	314.1	11 100	3700	1650
NS-O-(Me)$_3$	356.2	8700	3100	1500

^{a} For spectroscopic studies, the concentration of compounds was in the range: 5.5–7 × 10^{-5} mol dm^{-3}.

Table 2 Electrochemical and thermodynamic properties of 1-amino-4-methyl-6-styrylnaphthalene-2-carbonitrile derivatives in the photo-oxidation and photo-reduction mechanism

Acronym	E_{00} [eV]	E_{ox} vs. Ag/AgCl [mV]	$\Delta G_{ox}{}^a$ [eV]	E_{red} vs. Ag/AgCl [mV]	$\Delta G_{red}{}^a$ [eV]	K_{SV} [M^{-1}]
NS	2.78	1167	−0.97	−1840	−0.07	86.6
NS-Me	2.92	1099	−1.18	nd	nc	81.4
NS-F	2.88	1350	−0.88	nd	nc	39.8
NS-Cl	2.89	1107	−1.13	nd	nc	73.6
NS-CN	2.78	1122	−1.02	−1603	−0.31	67.2
NS-S-Me	2.90	1150	−1.11	nd	nc	155.4
NS-O-Me	2.94	1180	−1.12	nd	nc	254.7
NS-O-(Me)$_3$	2.94	1107	−1.19	−1577	−0.44	407.2

^{a} Calculated from the classical Rehm–Weller equation: $\Delta G_{et} = F[E_{ox}(D/D^{•+}) - E_{red}(A^{•-}/A)] - E_{00} - \left(\dfrac{N_A e^2}{4\pi\varepsilon_0\varepsilon_r a}\right)$. E_{ox} (D/D$^+$) – electrochemically determined oxidation potential of the electron donor (0.864 V for amine MDEA vs. Ag/AgCl). E_{red} (A$^{•-}$/A) – electrochemically determined reduction potential of the electron acceptor (−0.64 V for the diphenyliodonium salt vs. Ag/AgCl).[66,67] E_{00} – singlet state energy of the sensitizer determined based on excitation and emission spectra (Fig. S20–S27 in ESI). nd – not detected. nc – not calculated.

iodonium salt quencher. The efficiency of the proposed systems was determined empirically by analyzing the kinetics of the free-radical and cationic photopolymerization processes.

3.3. Cationic photopolymerization initiating capability

Cationic photopolymerization is a living process that can continue even after light exposure is ceased. Another advantage of this process is its resistance to oxygen inhibition and the large number of raw materials that can be used as monomers. The proposed photoinitiating systems in the form of 1-amino-4-methyl-6-styrylnaphthalene-2-carbonitrile derivatives and diaryliodonium salts (IOD) were tested for their ability to initiate the cationic ring-opening polymerization of the CADE monomer. Measurements were carried out using a Vis-LED emitting light with a wavelength of 405 nm and an intensity of $I_0 = 11.9$ mW cm^{-2}. Monomer conversion was determined from eqn (3), monitoring the reaction progress at 790 cm^{-1}, corresponding to the oxirane rings that undergo photopolymerization. The time dependency plots of the CADE monomer conversion are shown in Fig. 5.

The proposed two-component systems were able to initiate the cationic polymerization of the epoxy monomer CADE, resulting in monomer conversions of 30–60%. The highest conversion was achieved by using 1-amino-6-[(E)-2-(4-fluorophenyl)vinyl]-4-methylnaphthalene-2-carbonitrile (NS-F), which contains a fluorine substituent. High conversions were also obtained for other photosensitizers with strong electron-donor groups, such as thiomethoxyl or methoxyl substituents (NS-O-Me, NS-O-Me, and NS-O-(Me)$_3$). In contrast, the system containing 1-amino-4-methyl-6-[(E)-2-(4-methylphenyl)vinyl]naphthalene-2-carbonitrile (NS-Me) with an electron-donor methoxyl group showed the highest photopolymerization rate. The final conversion of the CADE monomer and the kinetic parameters of the process, such as induction time and photopolymerization rate, are summarized in Table 3.

3.4. Free-radical photopolymerization initiating capability

The developed two-component initiating systems could also initiate a free-radical polymerization reaction. Their efficiency was tested on the Ebecryl® 4858, which is a low viscosity
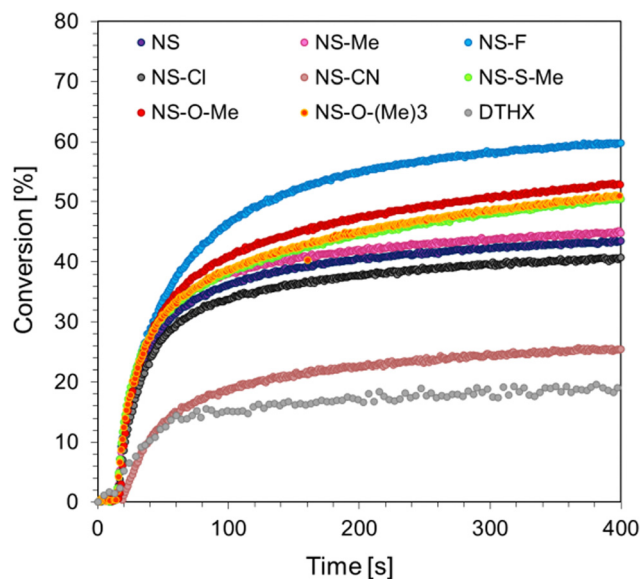

Fig. 5 Cationic photopolymerization profiles (epoxy function conversion vs. irradiation time) were determined using a two-component photo-initiating system based on IOD (1 wt%) and 1-amino-4-methyl-6-styrylnaphthalene-2-carbonitrile derivatives (0.1 wt%) under irradiation at 405 nm, I_0 = 11.9 mW cm^{-2}.

aliphatic urethane diacrylate. Free-radical photopolymerization is an important process in polymer chemistry because of the wide availability of acrylate and methacrylate monomers, which exhibit high reactivity. This process is initiated by free radicals, including those formed by the photo-fragmentation of an IOD cationic initiator in the presence of a sensitizer. The efficiency of the diaryliodonium salt–naphthalene–stilbene derivatives was studied under oxygen-free conditions, and the degree of conversion was monitored by observing the FTIR peak at 1635 cm^{-1}, corresponding to the C=C double bond. The following composition was tested: naphthalene–stilbene derivative (0.1 wt%), IOD initiator (1.0 wt%), and Ebecryl® 4858 monomer. The concentrations of the initiating system were related to the monomer's weight. A composition consisting only of the IOD initiator (1.0 wt%) and Ebecryl® 4858 monomer

Table 3 Summary of functional group conversions of CADE monomer and other kinetic parameters during cationic polymerization using a photoinitiating system based on bis-(4-*t*-butylphenyl)iodonium hexafluorophosphate (IOD) and 1-amino-4-methyl-6-styrylnaphthalene-2-carbonitrile derivatives

Acronym	Conversion[a] [%]	dC/dt[b] [s^{-1}]	Induction time[c] [s]
NS	46	0.97	8
NS-Me	47	1.29	10
NS-F	62	1.24	10
NS-Cl	43	1.04	11
NS-CN	27	0.50	14
NS-S-Me	56	1.12	8
NS-O-Me	58	1.15	10
NS-O-(Me)$_3$	57	1.26	10
DTHX	19	0.47	13

[a] Conversion – conversion, determined from eqn (3). [b] dC/dt – the slope of the kinetic curve representing the rate of the reaction, calculated as the derivative of the conversion after time. [c] Induction time – the time from when the light source is turned on to when the abrupt increase of conversion is detected (not including the preceding 10 second dark period).

was used as a reference. The time profiles for the polymerization reaction of the Ebecryl® 4858 acrylic monomer under visible light irradiation at 405 nm and 415 nm are shown in Fig. 6a and b, respectively.

As shown, despite the significant viscosity of the Ebecryl® 4858 monomer under the given conditions, it was possible to carry out photopolymerization reactions. Considerably high degrees of conversion, up to 79%, were obtained using the developed photosensitizers. The best photoinitiating system was composed of a diaryliodonium salt (IOD) and a 1-amino-4-methyl-6-[(*E*)-styryl]naphthalene-2-carbonitrile (NS) sensitizer, which not only led to the highest conversion but also had the shortest induction time and the highest conversion rate. In contrast, the compound showing the weakest sensitization ability was 1-amino-6-[(*E*)-2-(4-fluorophenyl)vinyl]-4-methylnaphthalene-2-carbonitrile (NS-F). A complete summary of the kinetic data for the radical photopolymerization process is presented in Table 4.
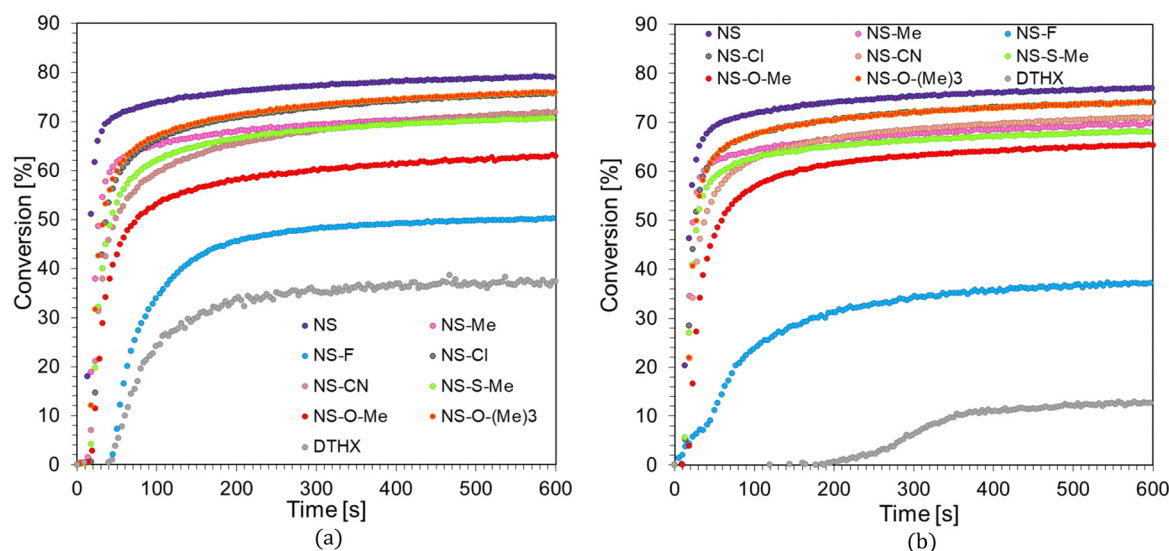

Fig. 6 Free-radical photopolymerization profiles (C=C double bond conversion *vs.* irradiation time) initiated using a two-component photoinitiating system based on IOD (1 wt%) and 1-amino-4-methyl-6-styrylnaphthalene-2-carbonitrile derivatives (0.1 wt%) under irradiation at (a) 405 nm, I_0 = 11.9 mW cm^{-2}; (b) 415 nm, I_0 = 14.1 mW cm^{-2}.

Table 4 Summary of the functional group conversions of Ebecryl4858® monomer and other kinetic parameters, using a photoinitiating system based on bis-(4-*t*-butylphenyl)iodonium hexafluorophosphate (IOD) and 1-amino-4-methyl-6-styrylnaphthalene-2-carbonitrile derivatives

Acronym	LED @405 nm			LED @415 nm		
	C[a] [%]	dC/dt[b] [s^{-1}]	Induction time[c] [s]	C[a] [%]	dC/dt[b] [s^{-1}]	Induction time[c] [s]
NS	79	5.72	10	77	5.13	9
NS-Me	71	3.11	12	69	4.96	12
NS-F	50	1.12	44	37	0.40	22
NS-Cl	76	2.84	16	74	4.27	11
NS-CN	72	1.84	10	71	4.30	14
NS-S-Me	71	2.39	15	68	2.95	9
NS-O-Me	63	1.86	16	65	2.05	15
NS-O-(Me)$_3$	76	2.85	12	74	3.31	11
DTHX	37	—	40	13	—	119

[a] C – conversion, determined from eqn (3). [b] dC/dt – the slope of the kinetic curve representing the rate of reaction, calculated as the derivative of the conversion after time. [c] Induction time – the time from when the light source is turned on to when the abrupt increase of conversion is detected (not including the preceding 10 second dark period).
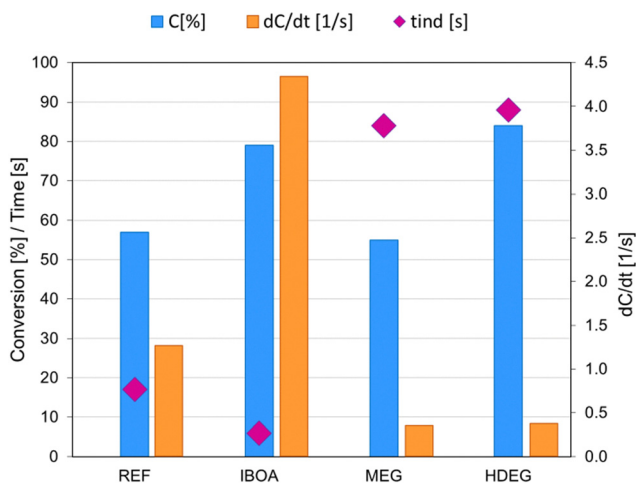
Fig. 7 Kinetic parameters for the arylate monomer determined from changes in the band with a maximum located at 1635 cm^{-1} for compositions containing different diluents; light source: LED at @405 nm (4.8 mW cm^{-2}).

3.5. Diluent effect

From an industrial point of view, using the above-tested Ebecryl® 4858 monomer is limited by its significant viscosity. Additionally, the high viscosity may compromise the homogeneity of the monomer-initiator mixtures, affecting both the initiating and overall efficiency of the photocuring process. Therefore, three diluents, reactive and non-reactive, were tested regarding their effect on viscosity, photopolymerization process (final conversion, conversion rate, induction time), and 3D printing. Four compositions differing only in the type of diluent were tested: (1) reference: Ebecryl® 4858 + IOD (3.0 wt%)/NS (0.1 wt%) (REF); (2) a reactive diluent reacting according to a free radical mechanism: Ebecryl® 4858/IBOA (0.7/0.3 w/w) + IOD (3.0 wt%)/NS (0.1 wt%) (IBOA); (3) non-reactive diluent: Ebecryl® 4858/MEG (0.7/0.3 w/w) + IOD (3.0 wt%)/NS (0.1 wt%) (MEG); (4) reactive diluent reacting according to the cationic mechanism: Ebecryl® 4858/HDEG (0.7/0.3 w/w) + IOD (3.0 wt%)/NS (0.1 wt%) (HDEG). The process was performed under the following conditions: 405 nm and intensity I_0 = 4.8 mW cm^{-2}. This intensity was chosen to correspond to the light intensity of the printer used in further studies. A graphical summary of the photopolymerization parameters for different mixtures of the Ebecryl® 4858 acrylate monomer

is shown in Fig. 7, and the quantitative data are summarized in Table 5.

The initiating system and its amount in the investigated formulations remain constant: IOD (3.0 wt%)/NS (0.1 wt%) (weights calculated in relation to the summed weight of the other components: monomer and diluent). Therefore, all the observed changes were related to the dilution and the diluent type. As shown, under the tested conditions (405 nm, 4.8 mW cm^{-2}), the undiluted reference sample (REF) had a C=C conversion of 57%, a conversion rate of 1.2 s^{-1}, and an induction time of 17 s. The addition of a diluent in the form of isobornyl acrylate (IBOA), which undergoes a free radical polymerization reaction, significantly accelerates the polymerization reaction – it is noticeable that the dConv./dt was higher, the induction time was shortened to 6 s, and the degree of double-bond conversion was increased, allowing the final C=C conversion to reach up to 79%. In contrast, adding ethylene glycol (MEG) as a non-reactive diluent decreased the kinetic parameters of the polymerization process. For the MEG sample, we observed a slight reduction in the conversion of double bonds, a slowed-down conversion rate, and an increased induction time of up to 84 s. A HDEG sample, using 1,6-hexanediol diglycidyl ether (HDEG), which is a reactive diluent reacting through a cationic mechanism, is a hybrid radical-cationic mixture leading to the preparation of Interpenetrating Polymer Networks (IPN). Adding HDEG to Ebecryl® 4858 monomer improved the C=C bond conversion, yielding 84% conversion of the acrylic monomer. In contrast, HDEG caused the most significant increase in induction time to 88 s and a significantly slower double-bond conversion. Among the investigated systems, the IBOA sample was found to be the best in terms of polymerization process parameters, where the IBOA monomer was used as a reactive diluent, reacting according to the same mechanism as the base monomer Ebecryl® 4858.

The effect of the diluent type was also determined by the rheological behavior during the photopolymerization reaction. The undiluted reference and three samples with the same initiating system: IOD (3.0 wt%)/NS (0.1 wt%) and different diluents were tested for dynamic viscosity time dependence through oscillatory studies (Fig. 8a). Moreover, a photorheological assessment was carried out using a LED light source emitting at 405 nm (intensity of 4.8 mW cm^{-2}). As shown, the initial viscosity of the tested samples follows the order: REF > HDEG > IBOA > MEG. It is worth noting that the diluents in

Table 5 Summary of the kinetic parameters of the polymerization process for samples containing Ebecryl 4858® acrylate monomer and various diluents

Acronym	PI system	Component 1 (70 wt%)	Component 2 (30 wt%)	C^a based on the C=C bond [%]	dC/dt^b [s^{-1}]	t_{ind}^{c} [s]
REF	IOD (3.0 wt%)/NS (0.1 wt%)	Ebecryl 4858	Ebecryl 4858	57	1.2	17
IBOA	IOD (3.0 wt%)/NS (0.1 wt%)	Ebecryl 4858	IBOA	79	4.12	6
MEG	IOD (3.0 wt%)/NS (0.1 wt%)	Ebecryl 4858	MEG	55	0.33	84
HDEG	IOD (3.0 wt%)/NS (0.1 wt%)	Ebecryl 4858	HDEG	84	0.35	88

^{a} C – conversion, determined from eqn (3). ^{b} dC/dt – calculated as the slope of the kinetic curve. ^{c} Induction time – the time elapsed from the switching on of the light source to the actual start of the reaction.
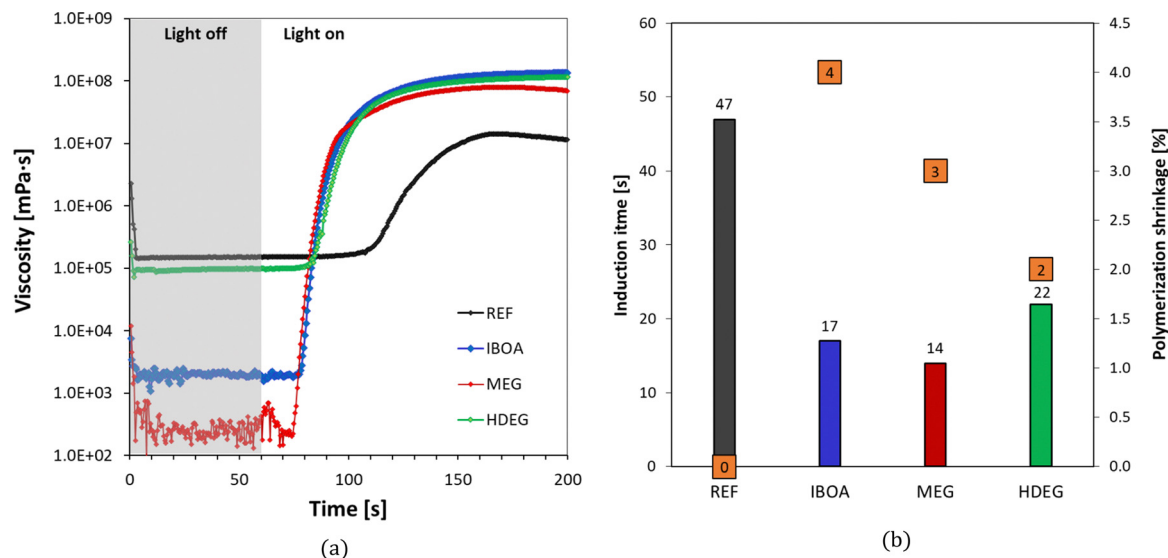
Fig. 8 (a) Storage modulus. G' *versus* irradiation time for formulations containing different diluents. Film thickness 100 μm, irradiation power 4.8 mW cm^{-2} (405 nm). (b) Photopolymerization parameters obtained from photorheological experiments. (REF) Ebecryl$^{\circledR}$ 4858 + IOD (3.0 wt%)/NS (0.1 wt%); (IBOA) Ebecryl$^{\circledR}$ 4858/IBOA (0.7/0.3 w/w) + IOD (3.0 wt%)/NS (0.1 wt%); (MEG) Ebecryl$^{\circledR}$ 4858/MEG (0.7/0.3 w/w) + IOD (3.0 wt%)/NS (0.1 wt%); (HDEG) Ebecryl$^{\circledR}$ 4858/HDEG (0.7/0.3 w/w) + IOD (3.0 wt%)/NS (0.1 wt%).

the different samples were added in equal percentages of 30% by weight. Parameters such as induction time, defined as the time between the light source being turned on (after 60 seconds dark period) and the abrupt increase in viscosity, were determined based on photorheological studies. The polymerization shrinkage was calculated using eqn (4). All parameters are presented in Fig. 8b. The induction time for the REF sample (Ebecryl$^{\circledR}$ 4858 monomer, no diluent) was the highest (47 s), whereas for the diluted samples it scaled in the order: HDEG > IBOA > MEG. Interestingly, it follows the same order as the viscosities, yet the undiluted reference clearly discontinued the trend (Fig. 8b). On the other hand, the most considerable polymerization shrinkage was observed for the IBOA sample, where the IBOA monomer, reacting according to the free-radical mechanism, was used as a diluent, and it was 4%. The undiluted sample (REF) showed no polymerization shrinkage under the measured conditions.

The present study also determined the diluent effect on the 3D printing process and the final properties of the obtained polymeric materials. The first step was to determine the critical parameters of 3D printing for the proposed formulations. Jacob's working curves were drawn to determine the critical energy (E_c) as the intersection of the graph with the x-axis and the penetration depth (D_p) as the slope of the curve for each of the tested compositions. The dependence of the cured sample's thickness on the exposure energy is shown in Fig. 9. Based on these values, each composition's printing parameters were determined and are summarized in Table S1 (ESI†). The highest critical energy is shown for the reference sample (REF) containing Ebecryl 4858 without diluent, correlating with its large induction time (Fig. 8). On the other hand, the lowest E_c was determined for dilution by non-reactive ethylene glycol (30% by weight). The highest conversion
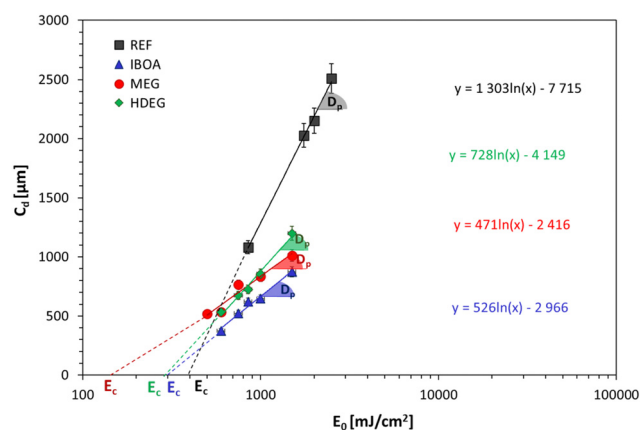

Fig. 9 Jacob working curves for compositions: (REF) Ebecryl$^{\circledR}$ 4858 + IOD (3.0 wt%)/NS (0.1 wt%); (IBOA) Ebecryl$^{\circledR}$ 4858/IBOA (0.7/0.3 w/w) + IOD (3.0 wt%)/NS (0.1 wt%); (MEG) Ebecryl$^{\circledR}$ 4858/MEG (0.7/0.3 w/w) + IOD (3.0 wt%)/NS (0.1 wt%); (HDEG) Ebecryl$^{\circledR}$ 4858/HDEG (0.7/0.3 w/w) + IOD (3.0 wt%)/NS (0.1 wt%).

(Table 5) was obtained for intermediate E_c (Samples: IBOA and HDEG), suggesting no direct link between these two properties.

3.5.1. Printing precision and printouts' properties. The influence of the solvent on the final parameters of three-dimensional materials obtained by 3D-VAT printing was also studied. Materials were printed based on the designed computer model (Fig. 3a) using the printing parameters listed in Table S1 (ESI†). An Anycubic Photon Ultra printer was used to print the models, and the optical properties of the resulting materials were analyzed using an Olympus optical microscope. The 2D images, height profiles of the printouts, and close-ups of the individual elements are shown in Fig. 10.
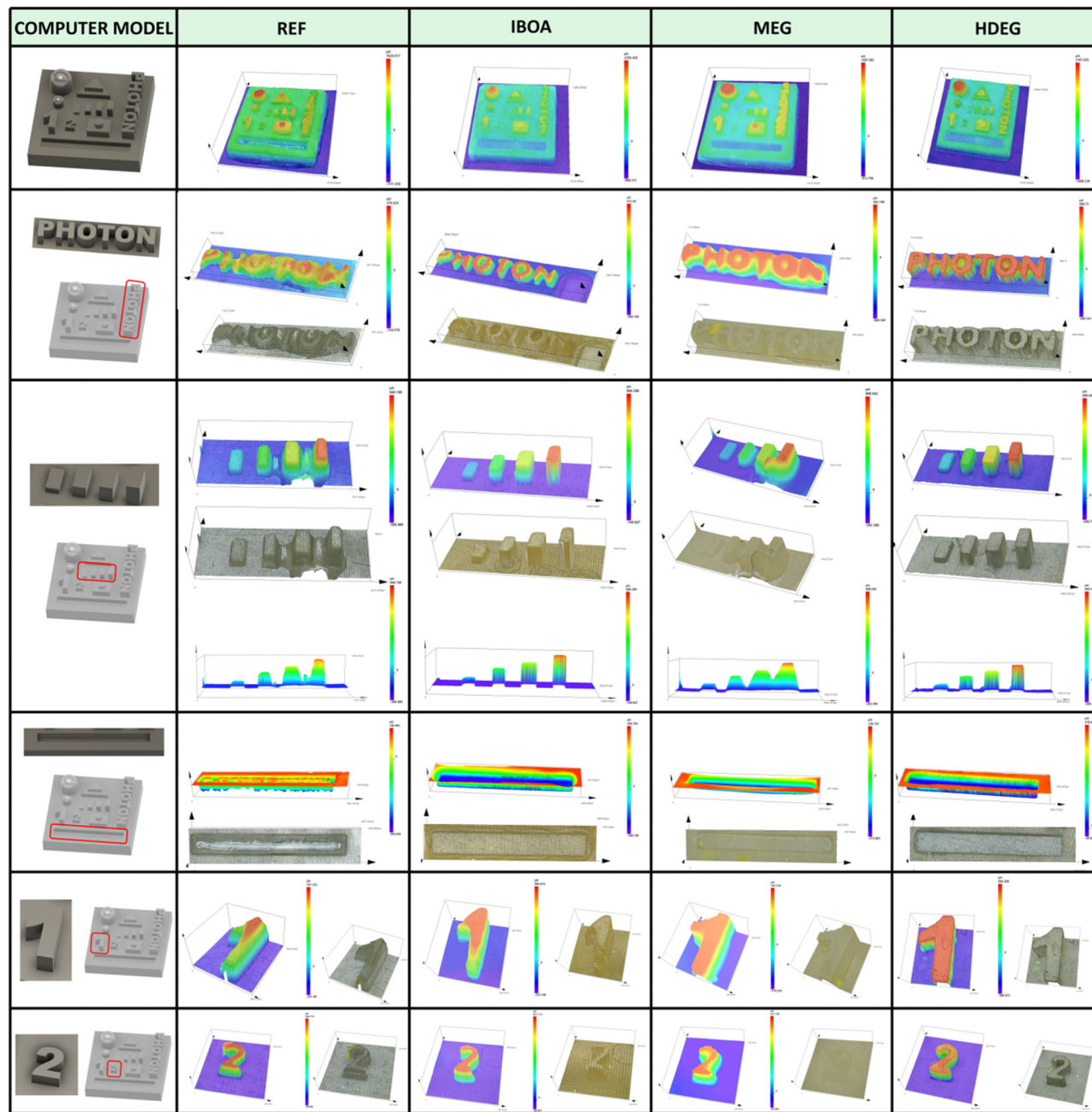
Fig. 10 Images of the final 3D printout obtained *via* DLP printing, using compositions containing different diluents: (REF) Ebecryl® 4858 + IOD (3.0 wt%)/NS (0.1 wt%); (IBOA) Ebecryl® 4858/IBOA (0.7/0.3 w/w) + IOD (3.0 wt%)/NS (0.1 wt%); (MEG) Ebecryl® 4858/MEG (0.7/0.3 w/w) + IOD (3.0 wt%)/NS (0.1 wt%); (HDEG) Ebecryl® 4858/HDEG (0.7/0.3 w/w) + IOD (3.0 wt%)/NS (0.1 wt%).

As shown, the use of acrylate monomer Ebecryl® 4858 alone leads to a material with poor resolution and printing precision, which is attributable, among other things, to the high viscosity of this monomer. Using diluents reduces the viscosity and changes the entire formulation's reactivity, altering the physical properties of the printed materials. The best printout regarding the printing resolution and accuracy was obtained for the reactive diluents, both free radical (IBOA) and cationic (HFDEG). On the other hand, the non-reactive diluent (MEG) led to swollen shapes with a low printing accuracy. This could

be expected from a resin with very low critical energy (Fig. 9), making it susceptible to over-polymerization.

The specimens for dynamic mechanical analysis (DMA) were printed vertically concerning their longer side using the same printing parameters (Table S1, ESI†). Images of the resulting printouts are shown in Fig. S63 (ESI†). The poor printing accuracy and high viscosity of the REF sample yielded numerous structural defects in the form of cavities and cross-sections. Such specimens could not be reliably measured and were excluded from mechanical testing. The remaining materials
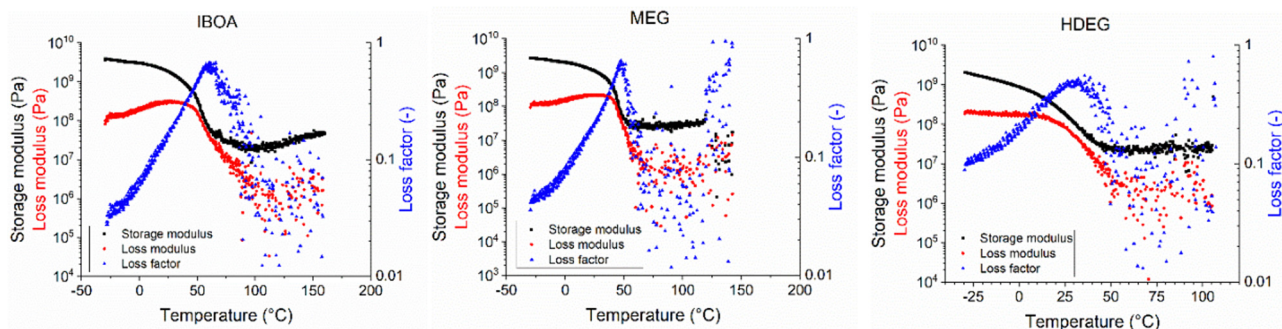
Fig. 11 Storage and loss moduli, and loss factor tan δ of the 3D printed samples as functions of temperature obtained using the DMA-HDT method.

Table 6 Summary of the parameters obtained from dynamic mechanical analysis for samples containing different diluents

Acronym	PI system	Component 1 (70 wt%)	Component 2 (30 wt%)	T_g	HDT (at 0.25 mm)	Maximum deflection	Temp. at break
IBOA	IOD (3.0 wt%)/NS (0.1 wt%)	Ebecryl 4858	IBOA	60.6	46.7	0.91	>160[a]
MEG	IOD (3.0 wt%)/NS (0.1 wt%)	Ebecryl 4858	MEG	47.7	40.6	0.40	119.7
HDEG	IOD (3.0 wt%)/NS (0.1 wt%)	Ebecryl 4858	HDEG	35.7	33.0	0.23	105.7

[a] Did not break within the tested temperature range.

were analyzed directly after the printing without any postcuring or extensive washing. The results of the dynamic mechanical analysis are shown in Fig. 11, and the experimental data are summarized in Table 6.

The storage modulus at room temperature, glass transition temperature (T_g), heat deflection temperature (HDT), maximum deflection, and temperature at brake scaled in the order IBOA > MEG > HDEG. All three samples showed the same rubbery plateau modulus of approx. 25 MPa in the 75–100 °C range, yielding a network density of 25 kmol m^{-3}. This means that the structure of the printed polymer network was insensitive to the diluent type. However, the IBOA sample increased the plateau modulus more than two times between 100 and 160 °C, denoting the increased network density to ≈ 42 kmol m^{-3}. This strengthening is attributed to the unreacted monomer thermally post-cured[30] during the measurement by the IOD photoinitiator decomposing at high temperatures.[68] Nevertheless, the diluent type greatly impacted the chain mobility, as apparent from the varied T_g. As expected, the highest T_g was found for IBOA, a reactive free-radical diluent, which can cure alongside the primary monomer. However, IBOA as a monofunctional monomer did not increase the network density nor prolong the chain length between the crosslinks, as suggested by the constant plateau modulus. On the other hand, MEG, despite being a non-reactive diluent, promoted the reaction rate more than the reactive HDEG. That was attributed to the lower viscosity of MEG and the generally slow conversion rate of cationic monomers. Moreover, MEG is a hydrogen donor, and such compounds may act as co-initiators in free-radical polymerization, potentially explaining the MEG sample's very low E_c (Fig. 9).[69]

The printouts from REF, IBOA, MEG, and HDEG samples were subjected to thermogravimetric analysis in the 25–700 °C range (Fig. 12). The thermal decomposition of the reference sample
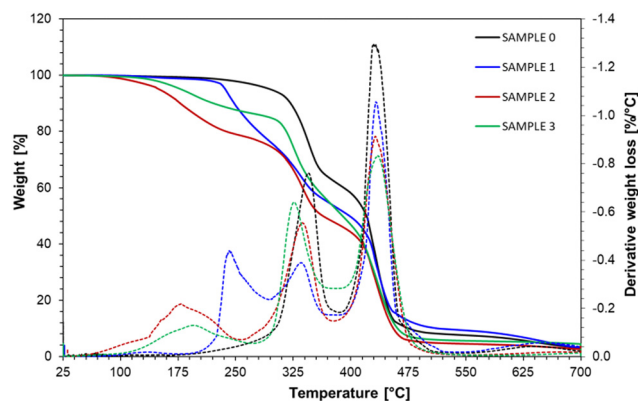

Fig. 12 Thermogravimetry results represented by weight and derivative weight loss signals as a function of temperature.

consists of two steps, while the diluted samples contain an additional weight-loss step at lower temperatures. The sample with the MEG non-reactive diluent started to lose weight already at 50 °C, marking the presence of loosely bonded solvent with a maximum evaporation rate detected at 178 °C. Analogically, the HDEG sample's maximum evaporation rate at 195 °C supports the conclusion that the HDEG remains largely uncured. The weight loss associated with this step was lower, only 15%, but HDEG could be thermally post-cured during the measurement. Finally, the IBOA sample had the highest thermal stability, up to 230 °C, among the diluted samples, as expected from a reactive diluent.

3.6. Preparation of nanocomposites using the developed initiating systems and resin based on acrylate monomers

As part of the search for the best formulation for 3D printing, several photoinitiating systems composed of a commercial

initiator in the form of diaryliodonium salt (IOD) and 1-amino-4-methyl-6-styrylnaphthalene-2-carbonitrile derivatives were tested within the scope of this manuscript. In addition, attempts were made to optimize the acrylate monomer Ebecryl® 4858 composition using various reactive and non-creative diluents. Based on the above studies, one formulation was selected to manufacture light-cured nanocomposites using additive technologies. For this purpose, the chosen composition used the IBOA diluent: Ebecryl® 4858/IBOA (0.7/0.3 w/w) + IOD (3.0 wt%)/NS (0.1 wt%) and two types of nano-additives: silver oxide (Ag$_2$O) at 1, 2, and 5 wt% relative to the weight of the monomers and hydroxyapatite (HA) in amounts of 2, 5, and 10%. The *in situ* polymerization process was studied using real-time FTIR and photorheology techniques, and the developed materials' 3D-VAT printing process and final properties were analyzed.

3.6.1. Real-time study of the kinetics of the photopolymerization process of nanoresins. Because the photopolymerization of resins containing functional nano-additives is compromised, searching for effective photoinitiating systems that can counteract the unfavorable behavior of these nanometric additives in light-cured compositions is still ongoing. To understand the photopolymerization process leading to nanocomposites both *in situ* and using 3D-VAT printing, various nano-additives have been studied, including silver oxide, whose color results in greater light absorption relative to the initial formulation, and hydroxyapatite, which, unlike Ag$_2$O, scatters light applied to the sample. However, in both cases, the presence of an additive at the nanometer scale is a challenge, particularly for applying such nanresins in 3D printing. The first step of this study was to analyze the kinetics of the photopolymerization process using real-time FTIR (Fig. 13). The measurements were conducted under oxygen-limited conditions for 600 s at a constant temperature of 25 °C. The progress of the photopolymerization reaction was monitored at a band maximum located at 1635 cm^{-1}, corresponding to the C=C bond. The kinetic profiles of the radical photopolymerization process for the Ebecryl® 4858/IBOA composition (7/3, w/w), the initiating system IOD (3.0 wt%)/NS (0.1 wt%) and different contents of the nanoadditives are shown in Fig. 13a and b, and the values of the polymerization parameters determined from them are summarized in Table 7.

From the obtained results, it is clear that adding a nanofiller in the form of silver oxide and hydroxyapatite decreases the conversion of double bonds during photopolymerization; however, this effect is more pronounced for silver oxide. In the
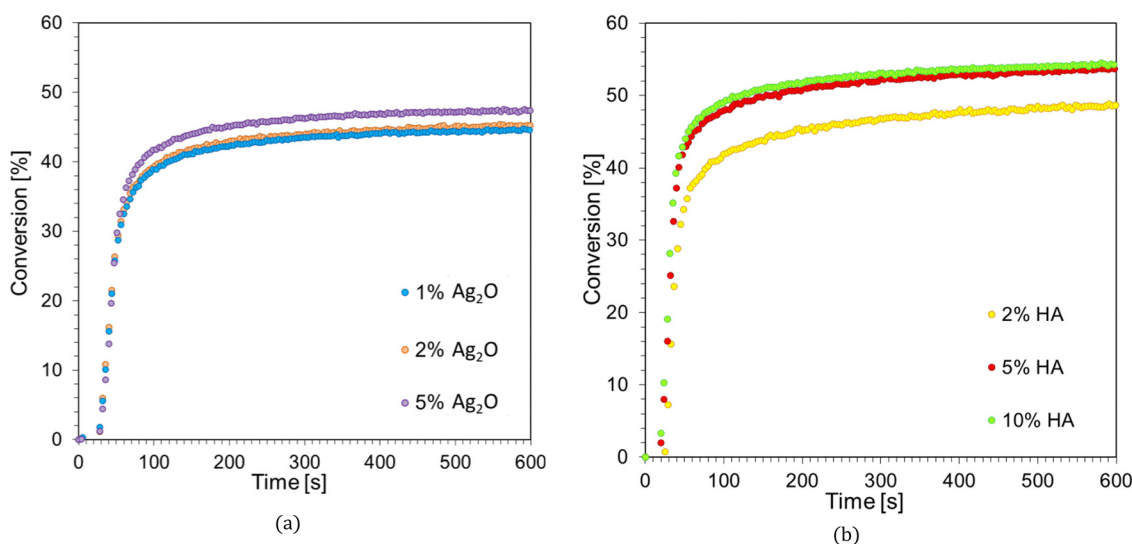

Fig. 13 Free-radical photopolymerization profiles (double bond conversion *vs.* irradiation time) initiated by a two-component photoinitiating system based on IOD (1 wt%) and 1-amino-4-methyl-6-styrylnaphthalene-2-carbonitrile derivatives (0.1 wt%) and mixture of monomers: Ebecryl 4858/IBOA (70/30 wt%) under irradiation at 405 nm. (a) Silver oxide (1;2;5 wt%); (b) hydroxyapatite (2; 5; 10 wt%).

Table 7 Summary of the functional group conversions of the Ebecryl 4858/IBOA (0.7/0.3 w/w) mixture, initiated using a two-component photoinitiated system: IOD (3.0 wt%)/NS (0.1 wt%), containing different types and concentrations of nanoadditives in the form of silver oxide (Ag$_2$O) or hydroxyapatite (HA)

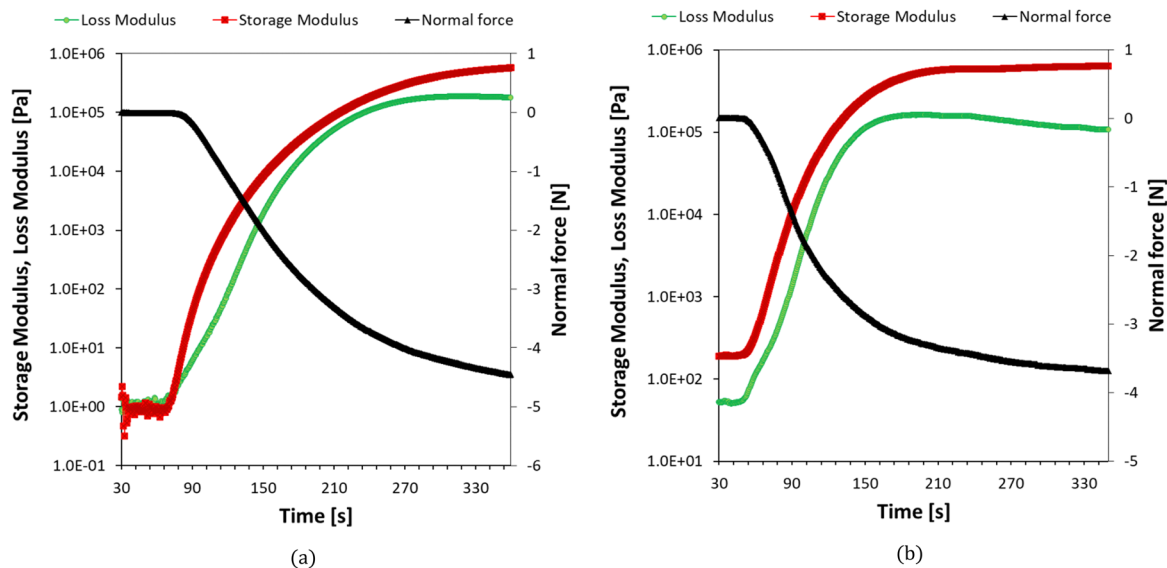| Acronym	Resin	Nanoadditive (weight %)	Conversion [%]	dC/dt [s^{-1}]	Induction time [s]
IBOA	Ebecryl 4858/IBOA (0.7/0.3 w/w)	—	79	4.12	6
1% Ag$_2$O		1% Ag$_2$O	45	0.74	14
2% Ag$_2$O		2% Ag$_2$O	44	0.73	15
5% Ag$_2$O		5% Ag$_2$O	47	0.72	16
2% HA		2% HA	48	1.06	12
5% HA		5% HA	53	1.32	13
10% HA		10% HA	54	1.36	17

Fig. 14 (a) The storage (red) and loss modulus (green) as well as normal force (black) as a function of the illumination time for SPOT LV nanoresin: Ebecryl® 4858/IBOA (0.7/0.3 w/w) + IOD (3.0 wt%)/NS (0.1 wt%) + 5% of Ag$_2$O. (b) The storage (red) and loss modulus (green) as well as normal force (black) as a function of the illumination time for SPOT LV nanoresin: Ebecryl® 4858/IBOA (0.7/0.3 w/w) + IOD (3.0 wt%)/NS (0.1 wt%) + 10% of HA. Film thickness 100 µm, irradiation power 4.8 mW cm^{-2} (405 nm), dark period: 60 s.
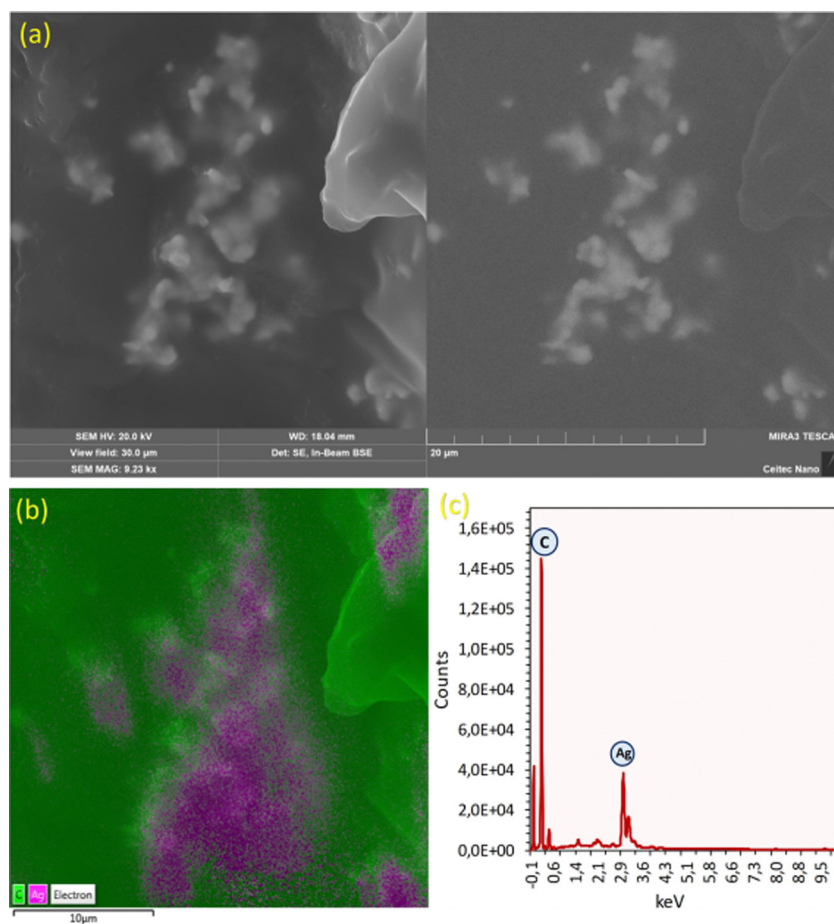

Fig. 15 SEM-EDS analysis silver oxide nanocomposite (Ebecryl® 4858/IBOA (0.7/0.3 w/w) + IOD (3.0 wt%)/NS (0.1 wt%) + 5% of Ag$_2$O: (a) SE morphology contrast images; (b) EDS map; (c) energy dispersive spectrum.

case of Ag$_2$O, 1% by weight resulted in a 34% reduction in monomer conversion, with a near-constant degree of conversion, prolonged induction time, and decreasing conversion rate with the increasing filler concentration (Table 7). A similar effect was evident when HA was used as a functional nanofiller. The addition of 2% HA resulted in a 31% reduction in double bond conversion during the photopolyprism reaction, and as with silver oxide, increasing conversion rate, induction time, and monomer conversion were observed with increasing amounts of the functional nano-additive. This behavior of both nano-additives suggests that besides their negative impact on light distribution, they may also have a photochemical effect on the photopolymerization process, which we will explore in our next article.

The photopolymerization of nanoresins containing different concentrations of silver oxide and hydroxyapatite was also studied by changing the viscosity of the polymerized system using photorheology. Example results showing changes in loss and storage modulus, as well as changes in normal force during photocuring of the nanoresins, are shown in Fig. 14a and b. For compositions containing silver oxide, it is possible to determine the gelation point for each process, defined as the point of intersection of the storage modulus (G') and loss modulus (G''). Even in the formulation containing 5% of the nanoadditive in the form of Ag$_2$O (Fig. 14a), it was possible to determine the gel point because the initial storage modulus was lower than the loss modulus. With time, both moduli increase, while the increase in the storage modulus is much faster, and the intersection of the two moduli indicates the beginning of the polymer network formation. As the concentration of Ag$_2$O in the samples increased, the time required to reach the gelation point increased, correlating with the slower curing rate (Table 7). On the other hand, the hydroxyapatite caused gelation between 2 and 5% concentrations by weight, preventing the gel-point determination. We note that these gels stem from the physical crosslinks formed by the particle-polymer interaction, not chemical bonds, as in the photopolymerization case. Nevertheless, the reaction proceeds even in the gel state, as shown by FTIR studies for a composition containing even 10% by weight of HA.

3.6.1. Printing of nanocomposites and morphological analysis of the obtained nanomaterials. All compositions based on Ebecryl$^{®}$ 4858/IBOA (0.7/0.3 w/w) + IOD (3.0 wt%)/NS (0.1 wt%) resin, containing functional nano-additives in the form of silver oxide (Ag$_2$O) and hydroxyapatite (HA) in different weight concentrations, were tested for the possibility of using these resins in 3D printing. A LumenX$^{+™}$ printer (CellInk) was used for this purpose, and the designed computer model shown in Fig. 3b was used for testing. The materials after the printing process, without additional physical processing, were analyzed using optical and scanning electron microscopy (on gold sputter-coated samples). Images from the scanning electron microscope are shown the ESI† in Fig. S64–S67. As shown by the results of SEM analysis and EDS analysis, the addition of silver oxide as a functionalized nanofiller leads to the formation of agglomerates in the resin if no stabilizers are added (Fig. 15).

On the other hand, nanocomposites containing hydroxyapatite did not show agglomerates on SEM analysis, making this additive applicable to the developed resins without the need to add a stablizer.

4. Conclusion

This manuscript presents newly developed compounds in the form of 1-amino-4-methyl-6-styrylnaphthalene-2-carbonitrile derivatives as highly effective photosensitizers for diaryliodonium salts (IOD). The proposed two-component initiating system effectively initiated both an epoxy monomer's cationic photopolymerization and an acrylate monomer's free-radical photopolymerization. Significantly, the presented systems are compatible with modern light sources used in many standard 3D printers, such as light-emitting diodes, which emit light from the safe visible range, with a wavelength of 405 nm and even 415 nm. The versatility of the proposed photoinitiating systems composed of iodonium salt and naphthalene–stilbene derivative allowed us to analyze the effect of different types of diluents on the *in situ* photopolymerization process and the properties of the three-dimensional materials obtained by 3D-VAT printing. Three types of diluents were investigated: reactive diluent reacting according to the free-radical mechanism (IBOA), non-reactive diluent (MEG), and reactive diluent reacting according to the cationic mechanism (HDEG). The mechanical and thermal properties of the materials obtained from these formulations were also investigated. Based on this study, the best composition was selected, where both the primary monomer (Ebecryl$^{®}$ 4858) and the diluent (IBOA) reacted according to the same mechanism (free-radical mechanism). This formulation, combined with nano-additives in the form of silver oxide (Ag$_2$O) and hydroxyapatite (HA), was then analyzed to determine the parameters of the photocuring process of the nanocomposites and the possibility of their use in 3D-VAT printing. Based on the analysis of the kinetics of the photopolymerization process of these photosensitive nano-resins, it was noted that the addition of the nano-filler decreased the conversion of the monomer compared to the resin without filler, reduced the reaction rate, and increased the induction time, and this effect was more pronounced for compositions containing silver oxide as the filler. Moreover, as the concentration of the nano-additive in the system increased, the process speed and monomer conversion increased, and the induction time decreased. This suggests that the proposed nano-additives in the form of silver oxide (Ag$_2$O) and hydroxyapatite (HA) may also have sensitizing properties.

To conclude, within the framework of this manuscript, we were able to obtain novel initiating systems which have been proven effective not only in photoinitiating *in situ* photopolymerization reactions, but also in 3D-VAT printing. The excellent performance of these systems in DLP printing reinforces our belief that the proposed photoinitiating systems based on naphthalene–stilbene photosensitizers are a safe alternative to single-component phosphine oxide-based photoinitiators,

which are being withdrawn due to negative health effects. Moreover, we have proposed a new nanoresin containing an IOD/naphthalene–stilbene-based initiating system and silver oxide/hydroxapatite as a functional nanofiller. We have demonstrated that the use of such resin enables us to obtain materials with a complex geometry, and characterized with a good optical resolution. Further studies will focus precisely on the development of these nanocomposite materials, and on investigating the sensitizing properties of the nano-additives.

Author contributions

Wiktoria Tomal: conceptualization; data curation; validation; methodology; funding acquisition; investigation; formal analysis; writing – original draft; writing – review and editing; Karolina Gałuszka: data curation; investigation; validation; writing – review and editing; Maciej Pilch: data curation; investigation; validation; Martina Korčušková: data curation; investigation; validation; Anna Chachaj-Brekiesz: organic synthesis; validation; Petr Lepcio: validation; resources; supervision; writing – review and editing; Joanna Ortyl: conceptualization; funding acquisition; investigation; methodology; supervision; validation; writing – original draft; writing – review and editing.

Data availability

Data will be made available on request.

Conflicts of interest

The authors declare no conflicts of interest.

Acknowledgements

References

1 Y. Yagci, S. Jockusch and N. J. Turro, *Macromolecules*, 2010, **43**, 6245–6260.

2 M. Sangermano, I. Roppolo and A. Chiappone, *Polymers*, 2018, **10**, 136.

3 W. Tomal, T. Świergosz, M. Pilch, W. Kasprzyk and J. Ortyl, *Polym. Chem.*, 2021, **12**, 3661–3676.

4 M. Sangermano, *Pure Appl. Chem.*, 2012, **84**, 2089–2101.

5 L. Pierau, C. Elian, J. Akimoto, Y. Ito, S. Caillol and D. L. Versace, *Prog. Polym. Sci.*, 2022, **127**, 101517.

6 F. Petko, A. Świeży and J. Ortyl, *Polym. Chem.*, 2021, **12**, 4593–4612.

7 J. Ortyl, M. Topa, I. Kamińska-Borek and R. Popielarz, *Eur. Polym. J.*, 2019, **116**, 45–55.

8 J. Ortyl, M. Galica, R. Popielarz and D. Bogdał, *Pol. J. Chem. Technol.*, 2014, **16**, 75–80.

9 E. Andrzejewska, Free radical photopolymerization of multi-functional monomers, *Three-Dimensional Microfabrication Using Two-Photon Polymerization: Fundamentals, Technology, and Applications*, William Andrew Publishing, Norwich, 2016, pp. 62–81.

10 X. Peng, M. Yao and P. Xiao, *Macromol. Chem. Phys.*, 2021, **222**, 2100035.

11 Y. H. Li and Y. C. Chen, *Polym. Chem.*, 2020, **11**, 1504–1513.

12 C. Kütahya, P. Wang, S. Li, S. Liu, J. Li, Z. Chen and B. Strehmel, *Angew. Chem., Int. Ed.*, 2020, **59**, 3166–3171.

13 T. Borjigin, M. Schmitt, Y. Zhang, B. Graff, F. Morlet-Savary, J. Lalevée, N. Giacoletto, A. Rico, H. Bidotti, M. Nechab, F. Dumur, P. Xiao, T. Borjigin, M. Schmitt, N. Giacoletto, A. Rico, H. Bidotti, M. Nechab, Y. Zhang, B. Graff, F. Morlet-Savary, P. Xiao, F. Dumur and J. Lalevée, *Adv. Mater. Interfaces*, 2023, **10**, 2202352.

14 J. Ortyl, P. Fiedor, A. Chachaj-Brekiesz, M. Pilch, E. Hola and M. Galek, *Sensors*, 2019, **19**(7), 1668.

15 S. E. Shim, H. Jung, H. Lee, J. Biswas and S. Choe, *Polymer*, 2003, **44**, 5563–5572.

16 N. De Alwis Watuthanthrige, M. L. Allegrezza, M. T. Dolan, A. J. Kloster, M. Kovaliov, S. Averick and D. Konkolewicz, *Angew. Chem., Int. Ed.*, 2019, **58**, 11826–11829.

17 B. Parnitzke, T. Nwoko, K. G. E. Bradford, N. De Alwis Watuthanthrige, K. Yehl, C. Boyer and D. Konkolewicz, *Chem. Eng. J.*, 2023, **456**, 141007.

18 V. Bellotti, C. Daldossi, D. Perilli, M. D'Arienzo, M. Stredansky, C. Di Valentin and R. Simonutti, *J. Catal.*, 2023, **428**, 115074.

19 M. Zhu, S. Wang, Z. Li, J. Li, Z. Xu, X. Liu and X. Huang, *Nat. Commun.*, 2023, **14**, 1–10.

20 J. Mosnáček and M. Ilčíková, *Macromolecules*, 2012, **45**, 5859–5865.

21 S. Dadashi-Silab, M. Atilla Tasdelen and Y. Yagci, *J. Polym. Sci., Part A: Polym. Chem.*, 2014, **52**, 2878–2888.

22 G. Acik, M. U. Kahveci and Y. Yagci, *Macromolecules*, 2010, **43**, 9198–9201.

23 K. Wang, J. Peña and J. Xing, *Photochem. Photobiol.*, 2020, **96**, 741–749.

24 L. Qiao, M. Zhou, G. Shi, Z. Cui, X. Zhang, P. Fu, M. Liu, X. Qiao, Y. He and X. Pang, *J. Am. Chem. Soc.*, 2022, **144**, 9817–9826.

25 J. Ortyl, J. Wilamowski, P. Milart, M. Galek and R. Popielarz, *Polym. Test.*, 2015, **48**, 151–159.

26 J. Ortyl, P. Milart and R. Popielarz, *Polym. Test.*, 2013, **32**, 708–715.

27 W. Tomal, H. C. Kiliclar, P. Fiedor, J. Ortyl and Y. Yagci, *Macromol. Rapid Commun.*, 2023, **44**, 2200661.

28 M. Topa-Skwarczyńska, M. Galek, M. Jankowska, F. Morlet-Savary, B. Graff, J. Lalevée, R. Popielarz and J. Ortyl, *Polym. Chem.*, 2021, **12**, 6873–6893.

29 J. Ortyl and R. Popielarz, *J. Appl. Polym. Sci.*, 2013, **128**, 1974–1978.

30 M. Štaffová, F. Ondreáš, J. Svatík, M. Zbončák, J. Jančář and P. Lepcio, *Polym. Test.*, 2022, **108**, 107499.

31 W. Tomal, D. Krok, A. Chachaj-Brekiesz, P. Lepcio and J. Ortyl, *Addit. Manuf.*, 2021, **48**, 102447.

32 M. Layani, X. Wang, S. Magdassi, M. Layani, X. Wang and S. Magdassi, *Adv. Mater.*, 2018, **30**, 1706344.

33 Y. Bao, *Macromol. Rapid Commun.*, 2022, **43**, 2200202.

34 Y. Li, W. Wang, F. Wu and R. K. Kankala, *Front. Mater.*, 2023, **9**, 1118943.

35 M. Shah, A. Ullah, K. Azher, A. U. Rehman, W. Juan, N. Aktürk, C. S. Tüfekci and M. U. Salamci, *RSC Adv.*, 2023, **13**, 1456–1496.

36 Z. Weng, X. Huang, S. Peng, L. Zheng and L. Wu, *Nat. Commun.*, 2023, **14**, 1–9.

37 A. Bucciarelli, X. Paolelli, E. De Vitis, N. Selicato, F. Gervaso, G. Gigli, L. Moroni and A. Polini, *Addit. Manuf.*, 2022, **60**, 103200.

38 A. Bagheri and J. Jin, *ACS Appl. Polym. Mater.*, 2019, **1**, 593–611.

39 I. Sachdeva, S. Ramesh, U. Chadha, H. Punugoti and S. K. Selvaraj, *Neural Comput. Appl.*, 2022, **34**, 17207–17229.

40 Y. Wang, Y. Wang, C. Mao and D. Mei, *Mater. Des.*, 2023, **227**, 111698.

41 I. Kim, S. Kim, A. Andreu, J. H. Kim and Y. J. Yoon, *Addit. Manuf.*, 2022, **52**, 102659.

42 E. Hola, M. Topa, A. Chachaj-Brekiesz, M. Pilch, P. Fiedor, M. Galek and J. Ortyl, *RSC Adv.*, 2020, **10**, 7509–7522.

43 E. Hola, M. Pilch, M. Galek and J. Ortyl, *Polym. Chem.*, 2020, **11**, 480–495.

44 A. Al Mousawi, C. Dietlin, B. Graff, F. Morlet-Savary, J. Toufaily, T. Hamieh, J. P. Fouassier, A. Chachaj-Brekiesz, J. Ortyl and J. Lalevée, *Macromol. Chem. Phys.*, 2016, **217**, 1955–1965.

45 F. Petko, M. Galek, E. Hola, M. Topa-Skwarczyńska, W. Tomal, M. Jankowska, M. Pilch, R. Popielarz, B. Graff, F. Morlet-Savary, J. Lalevee and J. Ortyl, *Chem. Mater.*, 2022, **34**, 10077–10092.

46 F. Petko, A. Świeży, M. Jankowska, P. Stalmach and J. Ortyl, *Polym. Chem.*, 2023, **14**, 3018–3034.

47 Y. Bao, N. Paunović, J.-C. Leroux, Y. Bao, N. Paunović and J.-C. Leroux, *Adv. Funct. Mater.*, 2022, **32**, 2109864.

48 L. A. Milton, M. S. Viglione, L. J. Y. Ong, G. P. Nordin and Y.-C. Toh, *Lab Chip*, 2023, **23**, 3537–3560.

49 W. Tomal and J. Ortyl, *Eur. Polym. J.*, 2022, **180**, 111588.

50 S. Nechausov, A. Ivanchenko, O. Morozov, A. Miriyev, I. Must, O. Platnieks, M. Jurinovs, S. Gaidukovs, A. Aabloo, M. Kovač and B. Bulgakov, *Addit. Manuf.*, 2022, **56**, 102895.

51 L. Rodríguez-Pombo, X. Xu, A. Seijo-Rabina, J. J. Ong, C. Alvarez-Lorenzo, C. Rial, D. Nieto, S. Gaisford, A. W. Basit and A. Goyanes, *Addit. Manuf.*, 2022, **52**, 102673.

52 J. Mauriello, R. Maury, Y. Guillaneuf and D. Gigmes, *Adv. Mater. Technol.*, 2023, 2300366.

53 E. J. Bailey and K. I. Winey, *Prog. Polym. Sci.*, 2020, **105**, 101242.

54 B. Le, J. Khaliq, D. Huo, X. Teng and I. Shyha, *J. Manuf. Sci. Eng.*, 2020, **142**, 1–57.

55 M. S. S. Kumar, C. P. Selvan, K. Santhanam, A. Kadirvel, V. Chandraprabu and L. Sampathkumar, *Adv. Mater. Sci. Eng.*, 2020, 2165855.

56 S. Quiles-Díaz, Y. Martínez-Rubí, J. Guan, K. S. Kim, M. Couillard, H. J. Salavagione, M. A. Gómez-Fatou and B. Simard, *ACS Appl. Nano Mater.*, 2019, **2**, 440–451.

57 X. Huang, C. Zhi, Y. Lin, H. Bao, G. Wu, P. Jiang and Y. W. Mai, *Mater. Sci. Eng., R*, 2020, **142**, 100577.

58 W. Tomal, A. Chachaj-Brekiesz, R. Popielarz and J. Ortyl, *RSC Adv.*, 2020, **10**, 32162–32182.

59 Q. Mu, L. Wang, C. K. Dunn, X. Kuang, F. Duan, Z. Zhang, H. J. Qi and T. Wang, *Addit. Manuf.*, 2017, **18**, 74–83.

60 M. Criado-Gonzalez, A. Dominguez-Alfaro, N. Lopez-Larrea, N. Alegret and D. Mecerreyes, *ACS Appl. Polym. Mater.*, 2021, **3**, 2865–2883.

61 N. Vidakis, M. Petousis, N. Michailidis, V. Papadakis, A. Korlos, N. Mountakis and A. Argyros, *Polymers*, 2022, **14**, 1903.

62 M. Korčušková, V. Sevriugina, F. Ondreáš, J. Svatík, W. Tomal, V. Vishakha, J. Ortyl and P. Lepcio, *Polym. Test.*, 2022, **116**, 107798.

63 F. Ondreas, P. Lepcio, M. Zboncak, K. Zarybnicka, L. E. Govaert and J. Jancar, *Macromolecules*, 2019, **52**, 6250–6259.

64 A. Medellin, W. Du, G. Miao, J. Zou, Z. Pei and C. Ma, *J. Micro Nanomanuf.*, 2019, **7(3)**, 031005.

65 W. Tomal, M. Pilch, A. Chachaj-Brekiesz, M. Galek, F. Morlet-Savary, B. Graff, C. Dietlin, J. Lalevée and J. Ortyl, *Polym. Chem.*, 2020, **11**, 4604–4621.

66 P. P. Romańczyk and S. S. Kurek, *Electrochim. Acta*, 2017, **255**, 482–485.

67 B. Strehmel, *Z. Phys. Chem.*, 2014, **228**, 129–153.

68 P. Lepcio, J. Daguerre-Bradford, A. M. Cristadoro, M. Schuette and A. J. Lesser, *Mater. Horiz.*, 2023, **10**, 2989–2996.

69 T. N. Eren, N. Okte, F. Morlet-Savary, J. P. Fouassier, J. Lalevee and D. Avci, *J. Polym. Sci., Part A: Polym. Chem.*, 2016, **54**, 3370–3378.